Large Eddy Simulations on Vertical Axis Hydrokinetic Turbines - Power coefficient analysis for various solidities

Nathanaël Guillaud, Guillaume Balarac, Eric Goncalves da Silva, Jeronimo Zanette

Large Eddy Simulations on Vertical Axis Hydrokinetic Turbines - Power coefficient analysis for various solidities

N Guillaud[a], G Balarac[b], E Goncalvès[c], J Zanette[a]

[a] *HydroQuest SAS, INOVALLIA, bâtiment B, 16 chemin de Malacher, 38240 Meylan, France*
[b] *Univ. Grenoble Alpes, CNRS, Grenoble INP, LEGI, 38000 Grenoble, France*
[c] *ISAE-ENSMA/CNRS, Pprime UPR 3346, 86961 Futuroscope Chasseneuil Cedex, France*

Abstract

Large Eddy Simulations (LES) are performed on a Vertical Axis Hydrokinetic Turbine (VAHT) at two different solidities, so as to enable a more complete physical description of the flow than for classic statistical calculations. To analyze the turbine performances, local quantities are defined to evaluate the contribution of the different turbine elements to the global VAHT power coefficient. For a deeper analysis of the major losses, the *real turbine* is also compared with an *ideal turbine* composed of only three infinite blades. It is observed that the ideal turbine with the lower solidity provides the best performance, but the losses due to the blade tips and the arms strongly increase for the real turbine at the same solidity. Consequently, for the considered real turbine, there is no clear gain to decrease the solidity. Simulations of the ideal turbine are performed for various solidities at their optimal Tip Speed Ratio (TSR) to study the evolution of optimal power coefficient as a function of solidity. A maximum power coefficient is obtained for a small value of the solidity. This is explained because the optimal TSR of this optimal solidity leads to angles of incidences on the blade which avoid a penalizing dynamic stall phenomenon but are high enough to produce an important positive torque The design of an efficient turbine has then to limit losses, to be able to use small solidity and then to avoid dynamic stall phenomenon by having a high optimal TSR.

Keywords: Vertical Axis Hydrokinetic Turbines; Tip Speed Ratio; Solidity; Large Eddy Simulations

1. Introduction

Tidal currents represent a large renewable energy resource concentrated in a few dozen sites in the world [1]. Vertical Axis Hydrokinetic Turbines (VAHT) are less expensive than traditional hydropower facilities. They are also faster to install and allow the exploitation of more sites due to the possibility to create taylor-made arrays of turbine within regions such as rivers, man-made channels or tidal straits where the local bathymetry focuses the flow [2]. Given the promise of VAHT technology, the investigation of their performance is of increasing interest to researchers and companies.

A key parameter of VAHT is the turbine solidity, which allows to characterize the blockage of the flow due to the presence of the turbine. In this work, the turbine solidity is defined as the ratio between the cumulated blade chord length and the turbine diameter,

$$\sigma = \frac{Nc}{2R},$$

with N the number of blades, c the blade chord and R the turbine radius. Note that slight difference can appear about the definition of this quantity, in literature. For example, Gosselin et al. [3] define the turbine solidity as Nc/R, whereas Shiono *et al.* [4] define the turbine solidity as $Nc/(2\pi R)$. The turbine solidity has a major impact on the turbine efficiency and on the turbine capacity to support hydrodynamic loads. The influence of the turbine solidity on the turbine power coefficient has

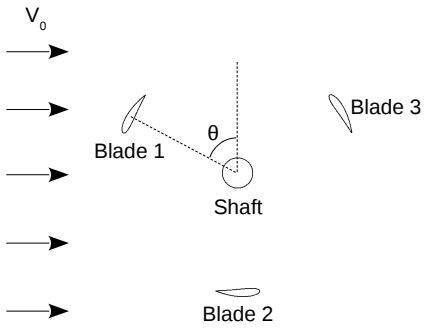

Figure 1: Top view of the VAHT for angular position definition.

been studied experimentally by Shiono *et al.* [4] and Blackwell *et al.* [5]. These studies show that for a given geometry, it exists an optimal solidity which maximizes the power coefficient of the turbine. This optimal solidity strongly depends on the turbine geometry. Shiono *et al.* [4] found an optimal solidity equals to 0.56, whereas Blackwell *et al.* [5] found a lower optimal solidity varying between to 0.2 and 0.25. An analyze of the causes of the obtained optimal solidity is not given in these studies. A first motivation of this present work is to deeper understand the influence of the turbine geometry details on the VAHT performances.

As observed by Shiono *et al.* [4] and Blackwell *et al.* [5], the turbine solidity influences the optimal Tip Speed Ratio (TSR). A higher solidity leads to a lower optimal TSR. The TSR λ is equal to $\frac{\omega R}{V_0}$, where ω is the turbine rotation speed magnitude and V_0 is the free-stream velocity. As described by Zanette [6], the TSR defines the relative flow incidence α on a VAHT blade. Considering a constant free-stream velocity accross the turbine, it can be shown that:

$$\alpha = \arctan\left(\frac{\sin(\theta)}{\cos(\theta)+\lambda}\right) \tag{1}$$

where θ is the angular position of the VAHT defined in Figure 1. The blade incidence is thus time dependent and periodic. As described by Paraschivoiu [7], at small TSRs, the static stall angle of incidence of the blade is exceeded and the dynamic stall phenomenon [8] occurs. As the optimal TSR of high solidity turbines is low, high solidity turbines operates with dynamic stall phenomenon at their optimal TSR. The dynamic stall phenomenon in VAHT has been observed in various experimental studies [8, 9, 10, 11, 12, 13]. This phenomenon is strongly influenced by the maximum angle of incidence and the reduced frequency of the blades [14]. A definition of the reduced frequency of the blades of a VAHT has been introduced by Laneville and Vittecoq [15]:

$$k_{VAHT} = \frac{\sigma}{N}\cdot\frac{1}{\lambda-1}\cdot\left(\arctan\left(\frac{1}{\sqrt{\lambda^2-1}}\right)\right)^{-1} \tag{2}$$

As shown by this equation, the reduced frequency and consequently the dynamic stall phenomenon in a VAHT is influenced by the TSR and the solidity of the VAHT.

Numerous numerical studies have been performed on VAHT. However, the flow in a VAHT and the associated turbine power coefficient are challenging to predict. Unsteady Reynolds Averaged Navier-Stokes (URANS) computations have been performed in 2D configurations by Pellone *et al.* [16] and Zanette [6] on high solidity VAHT ($\sigma = 0.55$). The classic bell-shape

of power coefficient as a function of TSR was reproduced with slight difference with experimental data. The flow topology at different TSRs was compared with measurements obtained from Particule Image Velocimetry (PIV) [17]. Whereas the numerical vorticity fields are coherent the dynamic stall vortex development is delayed in the simulations. The two-dimensional approach does not take into account the losses due to blade tips, arms and shaft. Consequently, the turbine power coefficient is largely overestimated. Three-dimensional URANS simulations were also performed by Pellone *et al.* [16] and Zanette [6]. The prediction of the turbine power coefficient was improved. However, the turbine power coefficient evolution with angular position still shows discrepancies compared with the experimental results and the dynamic stall vortex development is still delayed. Simulations on a high solidity VAHTs including blade tips, arms and shaft highlighted the high losses generated by blades tips and blade/arm connections at optimal TSR. Yet, the influence of the turbine solidity was not studied. Joo *et al.* [18] studied the influence of solidity of a VAHT by performing 3D URANS computations. The geometry is simplified and does not contain arms and shaft. The increase of the optimal TSR with a decrease of the solidity is found, as well as a solidity which maximize the power coefficient of the turbine. Authors highlight the impact of solidity on the flow blockage and the flow interaction between the blades and the free stream.

Posa *et al.* [19] investigated the wake of an isolated vertical axis wind turbine using large-eddy simulations. A filtered-structure fonction model and immersed boundary method was used. Losses due to blade tips, arms and shaft were not modeled as the studied geometry consists in three blades in rotation, with a periodicity condition applied in the rotation axis direction. Comparison with experimental data can therefore not be quantitative. However, ensemble averaged velocity profiles in the near wake of the turbine showed a good qualitative agreement with PIV measurements. Besides, the relative size and number of distinct structures in the wake of the turbine obtained by LES is in close agreement with experimental data. A numerical study involving both 2D and 3D URANS simulations and large-eddy simulations was led by Li *et al.* [20] on a vertical axis wind turbine. A $k-\omega$SST model and a dynamic Smagorinsky subgrid-scale model was used, respectively. The study case is a simplified geometry composed of three blades and a shaft, with a periodicity condition in the shaft direction. It does not take into account the losses due to blade tips and arms. The authors compared the evolution of the blade tangential force coefficient during a round with experimental results. Both URANS approaches delayed the dynamic stall and consequently overshot the tangential force in the region $0° < \theta < 180°$. The LES approach improved the prediction of the dynamic stall phenomenon and consequently improved the blade tangential force prediction. The prediction of turbine power coefficient is therefore improved by LES.

Even though its high computational cost, LES approach has shown its superior accuracy compared with RANS approach in various applications such as aerodynamic studies [21], combustion [22], meteorology [23], flow around hdyrofoil [24, 25], and architectural fluid mechanics [26] but also for less standard applications dealing for instance with accurate rain measurements [27], electronic system cooling design [28], sediment transport [29], or process engineering [30]. LES is then an attractive approach to capture the flow dynamics and to correctly predict the power coefficient of a vertical axis turbine. One of the main objectives of this work is then to perform the first LES of a complete VAHT geometry in order to deeply investigate the turbine performances and the influence of its solidity. Then, in this work, LES are performed on a complete three-blade VAHT, namely the Achard turbine [31]. A particular emphasis is placed on the impact of solidity on the performances, which is today partially understood. To analyze the turbine performances, the global power coefficient is investigated with the introduction of local quantities. These local quantities are defined as the contribution of various elements of the turbine to the global power coefficient. To evaluate the major losses generated by the real turbine, simulations of an ideal turbine composed

with only three infinite blades are also performed.

The paper is organized as follows: the next section 2 details the study cases (sec. 2.1), the analyzed quantities (sec. 2.2) and the numerical set up (sec. 2.3). Section 3 allows to confirm the reliability of the performed simulations by using classic verification (sec. 3.1) and validation (sec 3.2) procedures. The section 4 gives the results of this work by first analyzing the VAHT at two solidities (sec. 4.1). In this part "real" and "ideal" turbines are considered. Simulations of the ideal turbine are finally performed for various solidities at the optimal TSR to study the evolution of optimal power coefficient as a function of solidity (sec. 4.2). Conclusions are drawn in section 5 with a sum-up of the main mechanisms having an effect on the turbine performances.

2. Numerical methodology

2.1. Configurations studied

The considered geometry is an Achard turbine [31]. The first geometry considered is this work corresponds to the turbine experimentally studied by Dellinger [32] and Mentxaka Roa *et al.* [33]. This turbine is a Darrieus-type turbine composed by three blades, as shown in Figure 2. The blade section is a projected NACA0018 profile without pitch angle and the main characteristics of the turbine are summarized in table 1. This leads to a turbine with a solidity $\sigma = 0.55$, for which the optimal TSR is known from experimental data [32, 33], $\lambda_{opt} = 2$. Three TSRs are therefore considered, $\lambda = 1$, 2 and 2.5. To study the effect of solidity, this first geometry is modified to consider a second turbine with $\sigma = 0.16$. This modification is obtained by conserving the blade chord and by varying the turbine radius. For this new solidity, the optimal TSR can be estimated from experimental data compilation, showing that $\lambda_{opt} \propto 1/\sqrt{\sigma}$ [34]. The estimated optimal TSR for $\sigma = 0.16$ is then equal to 3.4. The three considered TSRs in this case are therefore 2.9, 3.4 and 3.9.

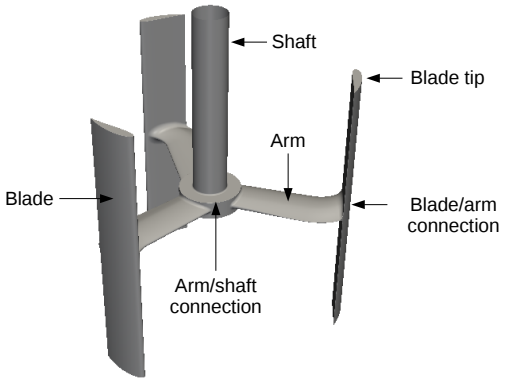

Figure 2: Illustration of the *real turbine* with $\sigma = 0.55$.

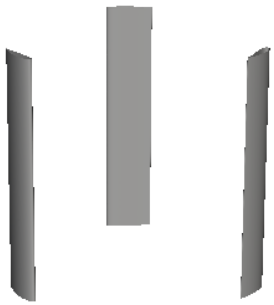

Figure 3: Illustration of the *ideal turbine* with $\sigma = 0.55$

Blade number	3
Turbine radius R	87.5mm
Blade chord c	32.1mm
Height H	175mm
Shaft diameter d	22mm

Table 1: Characteristics of the real turbine geometry.

These turbines are denoted as the *real turbines* in the following. To evaluate the major losses generated by these real turbines, *ideal turbines* only composed by three infinite blades are also considered, as shown in Figure 3. Then, the performance of these ideal turbines will not be affected by blade/arm connection, arm, shaft, blade tip, ... The same solidities and the same TSRs as the real turbines are considered. Finally, to investigate the evolution of the optimal turbine power coefficient of this ideal turbine as a function of its solidity, additional solidities 0.11, 0.34 and 1.08 are considered at the estimated optimal TSR, respectively 4.1, 2.3 and 1.3.

For all these turbines the free-stream velocity V_0 is set to 2.8 m/s, and the TSR is varied by changing the turbine rotation speed magnitude, ω. Considering all tested TSRs, this leads to a range of Reynolds number based on the chord length $Re_c = \frac{\omega R c}{\nu}$ (where ν is the water kinematic viscosity) varying between 8.9×10^4 and 3.7×10^5. Note that this Reynolds number variation is only due to the variation of ω, but at a given TSR, the Reynolds number is the same for all considered turbines, similarly to experiments.

2.2. Quantities of interest

To compare and study the different VAHTs, we introduce the mean and the instantaneous power coefficient $\left\langle C_p^{VAHT} \right\rangle$ and C_p^{VAHT} defined as:

$$\left\langle C_p^{VAHT} \right\rangle = \frac{\left\langle P^{VAHT} \right\rangle}{0.5\rho D H V_0^3} \quad ; \quad C_p^{VAHT} = \iint_{S_{VAHT}} C_p\left(\overrightarrow{OI}\right) dS \tag{3}$$

where $\left\langle P^{VAHT} \right\rangle$ is the mean power generated by the turbine equal to $\left\langle C_z^{VAHT} \right\rangle \omega$, where $\left\langle C_z^{VAHT} \right\rangle$ is the mean torque generated in the rotation axis direction. S_{VAHT} is the turbine surface and $C_p\left(\overrightarrow{OI}\right)$ is a local power coefficient generated by the point I of the turbine surface:

$$C_p\left(\overrightarrow{OI}\right) = \frac{C_z\left(\overrightarrow{OI}\right)\omega}{0.5\rho D H V_0^3} \tag{4}$$

$C_z\left(\overrightarrow{OI}\right)$ is the axial torque generated by the point I of the turbine:

$$C_z\left(\overrightarrow{OI}\right) = \left(\overrightarrow{OI} \wedge \left(-P\vec{n}_I + \overline{\overline{\tau}} \cdot \vec{n}_I\right)\right) \cdot \overrightarrow{e_z} \tag{5}$$

where P is the pressure, $\overline{\overline{\tau}}$ is the viscous stress tensor, $\vec{n}_I$ is the surface normal at the point I and $\overrightarrow{e_z}$ is the axial unit vector (turbine rotation axis direction).

To study the performances of different zones of the real turbines, the instantaneous power coefficient is integrated on parts of the turbine surface. A power coefficient is then defined for each region:

$$C_p^{region} = \iint_{S_{region}} C_p\left(\overrightarrow{OI}\right) dS. \tag{6}$$

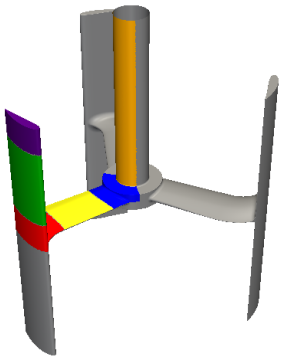

Figure 4: VAHT regions used for performance analysis
● : blade tip, ● : blade, ● : blade/arm connection,
● : arm, ● : arm/shaft connection, ● : shaft.
Only the upper symmetry of a blade is considered.

The considered VAHT regions are defined in Figure 4.

In order to compare the performance of the regions involving different heights, a region efficiency is introduced:

$$\eta^{region} = C_p^{region} \cdot \frac{H}{h^{region}} \tag{7}$$

where h^{region} is the height of the considered region.

The different variables presented in this section will be used to perform a detailed analysis of the VAHT performance. Layouts of $C_p\left(\overline{OI}\right)$ over the turbine surface will be shown. Isosurfaces of the Q-criterion [35] will also be shown to highlight the principal vortices of the flow.

2.3. Numerical set-up

To study the performance of these turbines, Large-Eddy Simulations (LES) of the flow configurations are performed. Conversely to URANS approach, LES allows to explicitly describe the turbulent motion at the largest scales of the flow [36]. It leads to a more complete physical description of the flow, but with a much higher computational cost than for classic statistical calculations. In this work, LES were performed using the YALES2 flow solver [37]. This code solves the incompressible and low-Mach number Navier-Stokes equations for turbulent flows on unstructured meshes using a projection method for pressure-velocity coupling [38]. It relies on fourth-order central finite-volume schemes and on highly efficient linear solvers [39]. The time integration is explicit for convective terms using a fourth-order modified Runge-Kutta scheme [40], with a semi-implicit integration for the diffusive terms. YALES2 solver is able to deal with unstructured grids composed only by tetrahedron elements or by prisms and tetrahedron elements, allowing to perform LES or DNS of complex geometries in the context of massively parallel computations. The solver has been validated for various applications such as combustion [41, 42], bio-mechanics [43], hydro-electricity [44], wind energy [45], or multiphase flows [46]. In this work, the equations are solved in a rotating frame and a rotating velocity condition is imposed at the inlet. A constant Courant-Friedrichs-Lewy (CFL) number of 0.9 is set for all cases. The Smagorinsky dynamic subgrid-scale model is used [47].

For both real and ideal turbines, the domain extension is equal to 16 turbine diameters around the VAHT to avoid confinement effect (see next section for a verification of this choice). A no-slip boundary condition is imposed on the turbine surface, with no wall laws. As no turbulence is imposed at the inlet, the flow is laminar upstream from the VAHT. The flow is assumed to be incompressible. Finally, for the real turbines, in the spanwise direction (rotation axis direction) the domain size is 1.43

turbine height as in the experiments [32, 33], and a slip-wall condition is used on top and bottom. For the ideal turbines, to represent infinite blades, the blades cross the domain and a periodicity condition is applied on top and bottom limits. For these cases, the domain height is set to $5c$. Computation domain and boundary conditions are illustrated in Figure 5 for the real turbine case with $\sigma = 0.55$.

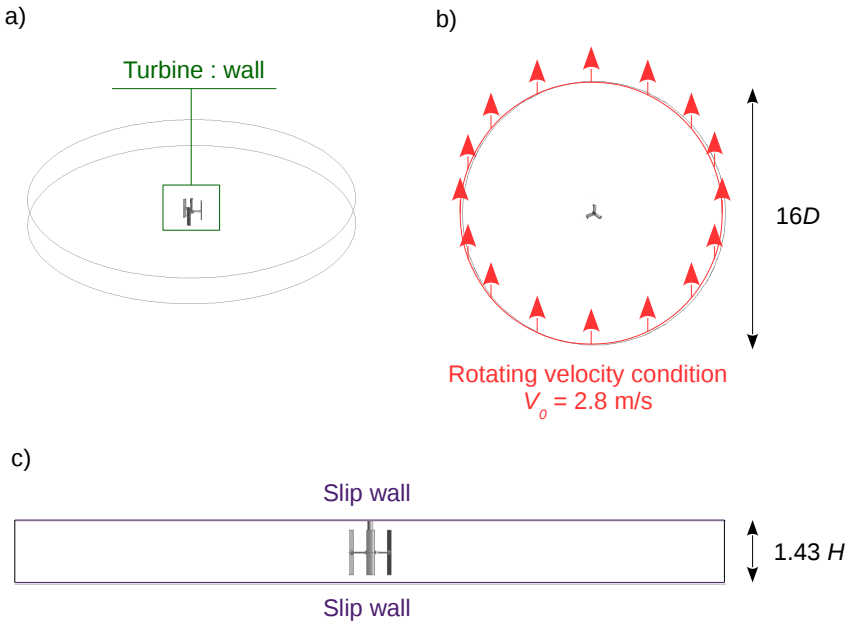

Figure 5: Illustration of the computation domain and boundary conditions for the real turbine case with $\sigma = 0.55$: (a) global view, (b) top view, (c) side view.

3. Verification and Validation of simulations

3.1. Verification: mesh convergence and confinement effect

To confirm the reliability of the performed simulations, a mesh convergence is first performed. The results for the real turbine case with $\sigma = 0.55$ is presented. Four meshes are generated with the same topology. The mesh is generated using 6 prism layers close to the turbines walls, and tetrahedrons elements elsewhere. The prisms layers are defined by the characteristics of the first layer (the closest layer to the turbine wall), i.e. by the length to the prism normal to the wall, Δn, and by its aspect ratio with the triangle base-length of the prism. Here, this ratio does not exceed 20, and the element growth rate from the wall is equal to 1.1. After the prism layers, tetrahedrons elements are used. In a first region defined with a radial extension equal to 6 turbine radius, the element size is limited to Δ_1. Outer this first region, the element size is limited to Δ_2. For the overall mesh, the growth rate is set to 1.1. The characteristics of the four meshes are summarized in table 2 and an illustration of the mesh M3 is given in Figure 6.

Mesh	Δn	Δ_1	Δ_2	Number of elements
M0	0.2 mm	80 mm	800 mm	16 million
M1	0.1 mm	40 mm	400 mm	29 million
M2	0.05 mm	20 mm	200 mm	54 million
M3	0.025 mm	10 mm	100 mm	105 million

Table 2: Characteristics of the considered meshes for the real turbine case with $\sigma = 0.55$.

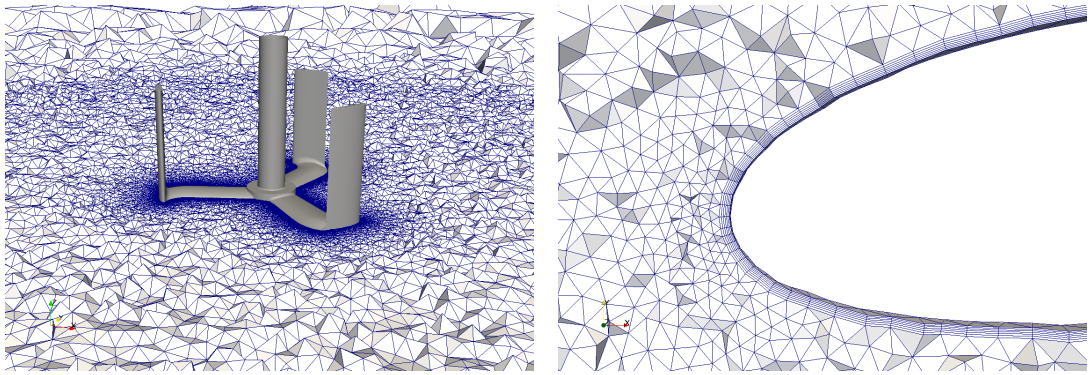

(a) Global view

(b) Zoom on a blade leading edge

Figure 6: Illustration of the mesh M3 for the real turbine case with $\sigma = 0.55$.

The evolution of the power coefficient for $\lambda = 2$ as a function of the turbine angular position, θ, is shown for the four meshes in Figure 7. Whereas a strong influence of the mesh is observed for the two coarser meshes (M0 and M1), the finer meshes (M2 and M3) are close. The result shows that the mesh independency is obtained for the finer mesh M3. Only this mesh will be considered in the following. Note that this mesh leads to a most likely value of the first cell size to the wall equals to 3 wall unit ($\Delta n^+ \approx 3$) along the turbine and is always smaller than 20 wall unit. This result is in agreement with other works [48].

Another verification step is to insure that the domain size is large enough to avoid that confinement effect affects the turbine performance. Then, three domain sizes have been tested: $4D$, $8D$, and $16D$, with D the turbine diameter (see Figure 5 for an illustration of the case with a domain extension of $16D$). Figure 8 shows the evolution of the power coefficient for $\lambda = 2$ for the three considered domain size. The case with a domain extension of $4D$ shows a strong effect of the confinement, with an over-estimation of the turbine performance. For the two other cases, the effect is smaller. A domain extension equals to 16 turbine diameters is therefore chosen.

Finally, to respect the mesh criteria and the ratio between the domain and the turbine diameters, the mesh is adapted for each geometries. The number of elements of each generated mesh is summarized in tables 3 and 4 for real and ideal turbines, respectively. It is then expected that LES approach leads to a more complete physical description of the flow, but with a much higher computational cost than for classic RANS calculations. For the final meshes, the CFL constraint leads to an angle variation in one time step around 5×10^{-3} degree. Then, for these meshes, a complete revolution of the turbine needs around 27h on 768 cores (Bull B720 Haswell, CPU frequency: 2.6 GHz).

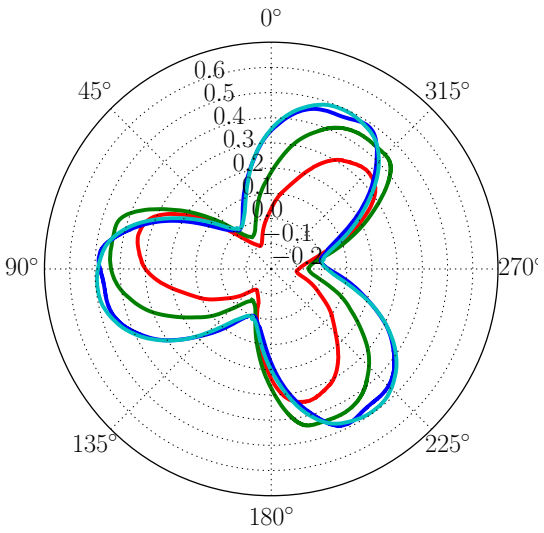

Figure 7: Power coefficient as a function of angular position for the real turbine with $\sigma = 0.55$ and $\lambda = 2$. Comparison of four meshes: M0 (——), M1 (——), M2 (——), and M3 (——).

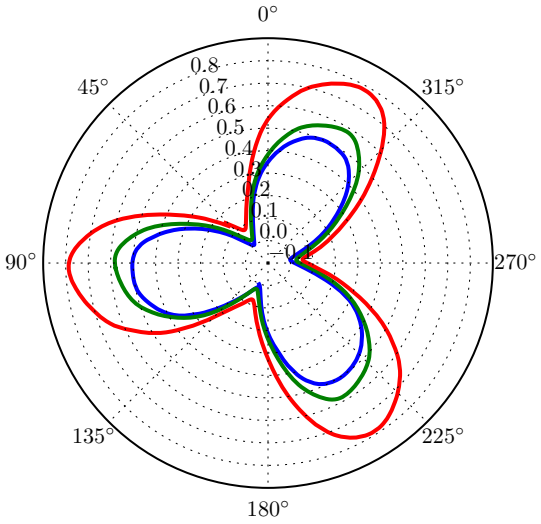

Figure 8: Power coefficient as a function of angular position for the real turbine with $\sigma = 0.55$ and $\lambda = 2$. Comparison of three domain extensions: $4D$ (——), $8D$ (——), and 16D(——).

σ	0.55	0.16
Mesh	105 M	177 M
λ	1 ; 2 ; 2.5	2.9 ; 3.4 ; 3.9

Table 3: Solidities, corresponding mesh element number (in million) and computed TSRs for LES of real turbines.

σ	1.08	0.55	0.34	0.16	0.11
Mesh	42 M	44 M	48 M	63 M	85 M
λ	1.3	1 ; 2 ; 2.5	2.3	2.9 ; 3.4 ; 3.9	4.1

Table 4: Solidities, corresponding mesh element number (in million) and computed TSRs for LES of ideal turbines.

3.2. Validation: comparison with experimental results

For validation, the real turbine with the solidity $\sigma = 0.55$ is now compared with experimental data obtained on a similar configuration for the three TSRs: $\lambda = 1$, 2, and 2.5. In experiments, PIV measurements have been performed to obtain the axial vorticity fields around a blade, and the instantaneous torque is obtained from a synchronous generator connected to the shaft (see [17, 32, 33] for details of the experimental set-up). It should be noted that the width of the experimental test section is only four times the turbine diameter, leading to confinement effect. As a consequence, the blockage ratio of the experimental configuration is four times higher than the numerical value. According to the work of Mentxaka Roa *et al.* [33], the turbine power coefficient decreases as the blockage ratio decreases. An estimation of the blockage effect on the mean power coefficient at the optimal TSR has been introduced by Werle [49], by defining the blockage ratio, ϵ, as the ratio of the cross-sectional areas between the turbine and the test section. The optimal mean power coefficient of two turbines for which the blockage ratio is ϵ_1 and ϵ_2 respectively follows the relation:

$$\langle C_p^{VAHT} \rangle (\epsilon_1) \approx \langle C_p^{VAHT} \rangle (\epsilon_2) \frac{(1-\epsilon_2)^2}{(1-\epsilon_1)^2} \tag{8}$$

Figure 9 shows the experimental and numerical mean power coefficients $\left\langle C_p^{VAHT} \right\rangle$ as a function of TSR. Numerical values

obtained with and without the blockage correction are presented for the optimal TSR. The classic bell-shaped curve of the mean power coefficient as a function of TSR is well reproduced. At the lower value $\lambda = 1$, the result obtained from LES is close to the experimental result. At this low rotation speed, the flow blockage led by the turbine is low and the influence of the test section area is small. The flow blockage increases with the turbine rotation speed. The influence of the test section area thus increases as the TSR increases. For the values $\lambda = 2$ and $\lambda = 2.5$, the blockage ratio influence is clearly observed. Numerical results using the correction show a very good agreement with the optimal experimental mean power coefficient. Note that the correction is only valid at the maximum power condition and then it can be only used for the optimal TSR [49].

Figure 10 depicts the evolution of the instantaneous VAHT power coefficient as a function of the turbine angular position θ for the three computed TSRs. At the solidity $\sigma = 0.55$ and $\lambda \geq 2$, a blade generates most of the power coefficient in the 60-120°zone. As the turbine is composed of three blades, the instantaneous turbine power coefficient shows three periodic zones corresponding to successive blades presence into the 60-120°zone. The evolution of the power coefficients as a function of the angular position is in good agreement with experimental data. The switch of the maximum power coefficient at approximately $\theta = 60°$ for $\lambda = 1$ instead of $\theta = 90°$ for $\lambda = 2$ and 2.5 is well predicted. Due to the difference of blockage ratio between the experimental and numerical configuration, the computed values of C_p^{VAHT} are lower than the experimental data, except for the lowest TSR value $\lambda = 1$. Note that the LES have also been qualitatively compared with experimental data obtained by PIV [50]. In particular, it has been shown that LES is able to reproduce the deep dynamic stall [51] observed for small TSR.

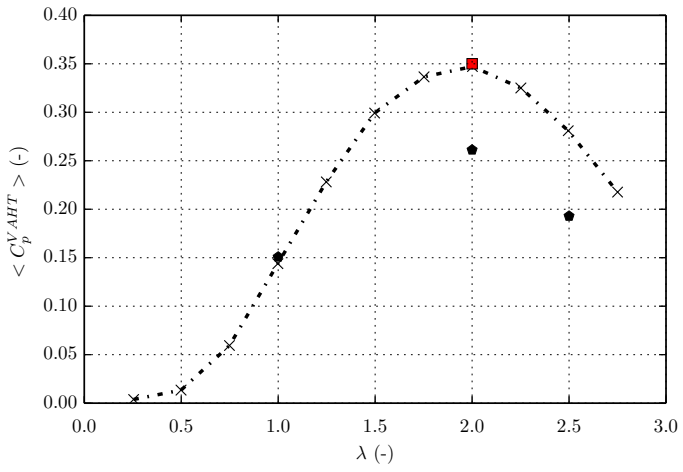

Figure 9: Mean power coefficient as a function of TSR. ⬟ : LES, ■ : LES with blockage ratio correction, — · —: experimental data extracted from [32].

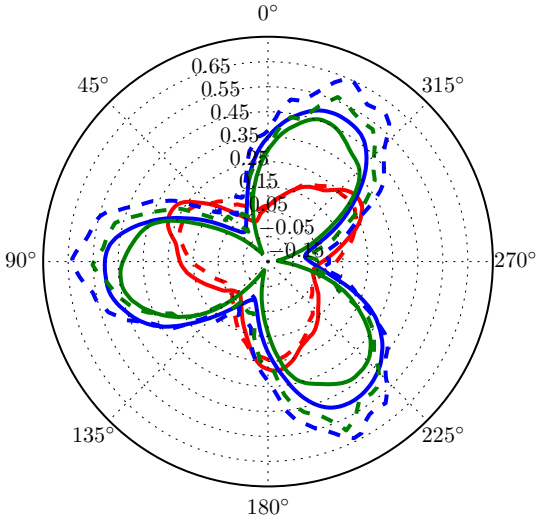

Figure 10: Power coefficient as a function of angular position. ——: $\lambda = 1$, ——: $\lambda = 2$, ——: $\lambda = 2.5$, ——: LES, – – –: experimental data extracted from [32].

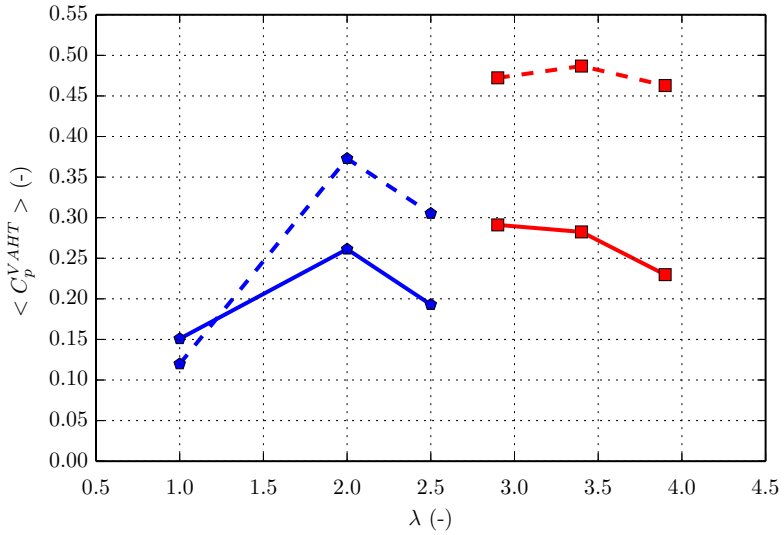

Figure 11: Mean power coefficient as a function of TSR.
⬟ : $\sigma = 0.55$, ■ : $\sigma = 0.16$ ——: real turbines, – – –: ideal turbine.

4. Results and discussion

4.1. Analysis of the VAHT at solidities $\sigma = 0.55$ and $\sigma = 0.16$

4.1.1. Mean power coefficients analysis

Figure 11 presents the mean power coefficients obtained for the real and ideal turbines at solidities $\sigma = 0.55$ and $\sigma = 0.16$, respectively. The results for the real turbines are depicted in plain lines while the results for the ideal turbines are depicted with dashed lines. As no losses are generated by blade tips, blade/arm connections, arms, arm/shaft connections and shaft, the power coefficients of the ideal turbines are strongly higher than those of the real turbines at the optimal TSRs (around 40% for the high solidity and 70% for the low solidity). The estimation of the optimal TSR for the low solidity turbine is correct for the ideal turbine. In the real turbines, the losses generated at high rotation speed lead to decrease the optimal TSR.

As regard to the solidity influence for the ideal turbine, the optimal mean power coefficient is 31% higher for the low solidity configuration. This difference is reduced to 8.1% when considering the real turbines. A low solidity VAHT can therefore produces a better power coefficient compared to a high solidity VAHT. However, low solidity turbines operates at higher TSR, which leads to increase losses and to limit the power coefficient gain. If the considered turbine geometry generates high losses, the power coefficient can be lower for the low solidity turbine.

The real Achard turbine has been designed with only one arm per blade in order to limit the losses. The blade/arm connection is also designed to limit the interactions between these two components. This leads the low solidity real turbine to have an optimal performance slightly higher than the high solidity real turbine.

The next sections are dedicated to the analysis of the differences of performance between the high and the low solidity turbines. We first propose a detailed analysis of the high solidity turbine performance at its optimal TSR. Then, a comparison between the high and the low solidity turbines will be made at their respective optimal TSRs.

4.1.2. Analysis of the high solidity turbine ($\sigma = 0.55$) at its optimal TSR ($\lambda = 2$)

The power coefficients and efficiencies as introduced in the section 2.2 for each region is now considered. At this solidity, the obtained regional power coefficients on the arm, arm/shaft connection and shaft are negligible and will not be reported here.

Figure 12 shows a global view of the flow through the real turbines. The main vortices are identified by plotting isosurfaces of the Q-criterion. The blade tip vortices are clearly illustrated.

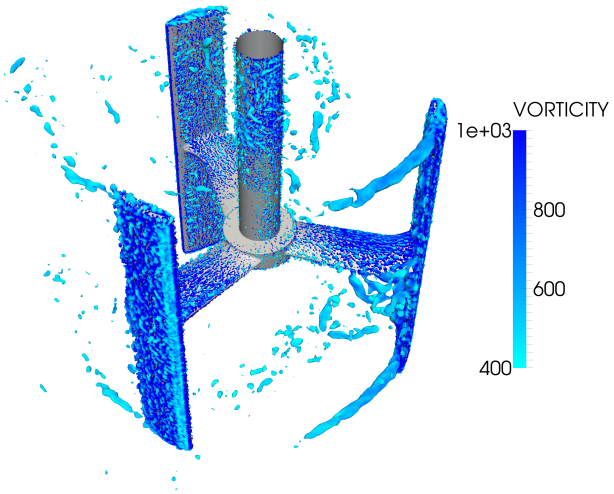

Figure 12: Isosurface of the Q-criterion, $Q = 2.25 \times 10^5 s^{-2}$, colored by vorticity magnitude (s^{-1}) for the real turbine at $\sigma = 0.55$ and $\lambda = 2$. The flow goes from right to left.

Figure 13 shows the evolution of C_p^{region} for the blade region, the blade tip region and the blade/arm connection region as a function of the angular position θ. At a solidity $\sigma = 0.55$, a blade generates most of the power coefficient in the upstream half-disk ($[0° \leq \theta \leq 180°]$). The blade generates few power coefficient in the downstream half-disk and can even produce negative torque. Figure 14 shows a contour of absolute velocity magnitude on a plane located at quarter-blade height. The high solidity of the VAHT leads to a high flow blockage and the flow velocities observed in the downstream half-disk ($[180° \leq \theta \leq 360°]$) are low. Few energy is then available after the flow goes through the upstream blades. The low velocity leads the angles of incidence on the blades to be close to 0°. It explains that the regional power coefficients can reach negative values in the downstream half-disk. As a consequence, the estimation of the flow incidence on the blades given by equation 1 is no more correct in the downstream half-disk. However, it remains a good approximation in the upstream half-disk. According to equation 1, the maximal angle of incidence on a blade at $\lambda = 2$ is close to 30°. This angle of incidence is strongly higher than the static stall angle of incidence of the blade. According to equation 2, at $\sigma = 0.55$ and $\lambda = 2$ the blade reduced frequency k_{VAHT} is equal to 0.35. These high reduced frequency and angle of incidence show that the blade operates with a dynamic stall phenomenon in the upstream half-disk.

To better understand the evolution of the power coefficient of the blade region in the upstream half-disk, the axial vorticity field at the vicinity of a blade is shown in Figure 15. At the revolution beginning, the angle of incidence on the blade increases and the flow seems to be entirely attached to the blade even when the static stall angle is exceeded (cf. Figure 15, $\alpha \approx 20.5°$, $\theta = 65°$). The power coefficient generated by the blade increases with the incidence. Then, the angle of incidence on the blade

continues to increase and the flow starts to detach from the trailing edge toward the leading edge (cf. Figure 15, $\alpha \approx 29.0°$, $\theta = 105°$). As seen in Figure 13, the instantaneous power coefficient generated by the blade region starts to decrease whereas the angle of incidence on the blade still increases. The blade hydrodynamic performance thus decreases. At the very beginning of the downstroke phase (cf. Figure 15, $\theta = 125°$, $\alpha \approx 29.9°$), the separation of the boundary layer is maximal and has nearly reached the blade leading edge. In the rest of the downstroke phase, the boundary layer reattaches to the blade from the leading edge toward the trailing edge. As seen in Figure 13, the instantaneous power coefficient of the blade region decreases with the angle of incidence on the blade.

The reduced frequency at this TSR and at this solidity leads the blade to operate with a dynamic stall phenomenon, which leads to benefit from the high incidences reached by the blade. A high amount of power is generated in the upstream half-disk, even if the lift-to-drag ratio of the blade is slightly decreased by the dynamic stall phenomenon.

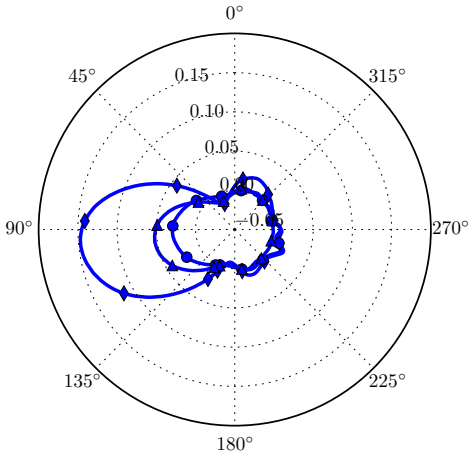

Figure 13: C_p^{region} as a function of angular position for the real turbine at $\sigma = 0.55$ and $\lambda = 2$. ♦: blade, ●: blade tip, ▲: blade/arm connection.

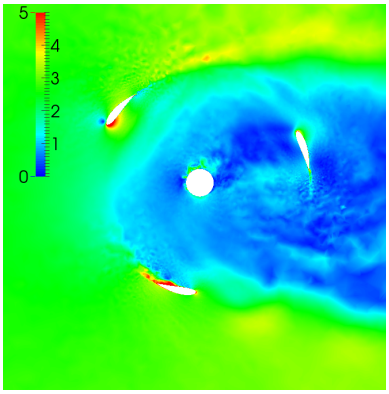

Figure 14: Slice of the computation domain at quarter-blade height colored by absolute velocity magnitude ($m.s^{-1}$) for the real turbine at $\sigma = 0.55$ and $\lambda = 2$.

Although all regions generate the major part of the power in the upstream half-disk, Figure 13 shows that the contributions of each region are unequal. The blade region generates the major part of the power coefficient. The different heights of the regions partialy explain these discrepancies. However, Figure 16 shows that the efficiency of the blade tip and the blade/arm connection are lower than that of the blade region. As seen in Figure 17, the blade tip vortex directly impacts the $C_p\left(\overline{OI}\right)$ distribution. The blade tip causes a leak of flow streamlines due to the difference of pressure between the pressure side and the suction side of the blade. A lift loss and consequently a local decrease of $C_p\left(\overline{OI}\right)$ is observed at the blade tip leading edge (cf. Figure 17a). The generated vortex also generates a brake area on the suction side at the blade tip trailing edge vicinity. The important lack of efficiency of the blade tip compared to the other regions appears in the upstream half-disk, where the pressure difference between the pressure side and the suction side is high. In the downstream half-disk, the blade tip vortices are weak as it can be seen in Figure 12. Figure 17a shows that the lack of efficiency of the blade/arm connection region seems to be firstly due to a lift loss at the leading edge. The arm deflects the flow streamlines towards up and down directions. The flow streamlines are consequently not perpendicular to the blade and the lift generated by the blade is degraded. Secondly, interferences between boundary layers of the blade and the arm lead to a brake area at the rear part of the blade/arm connection.

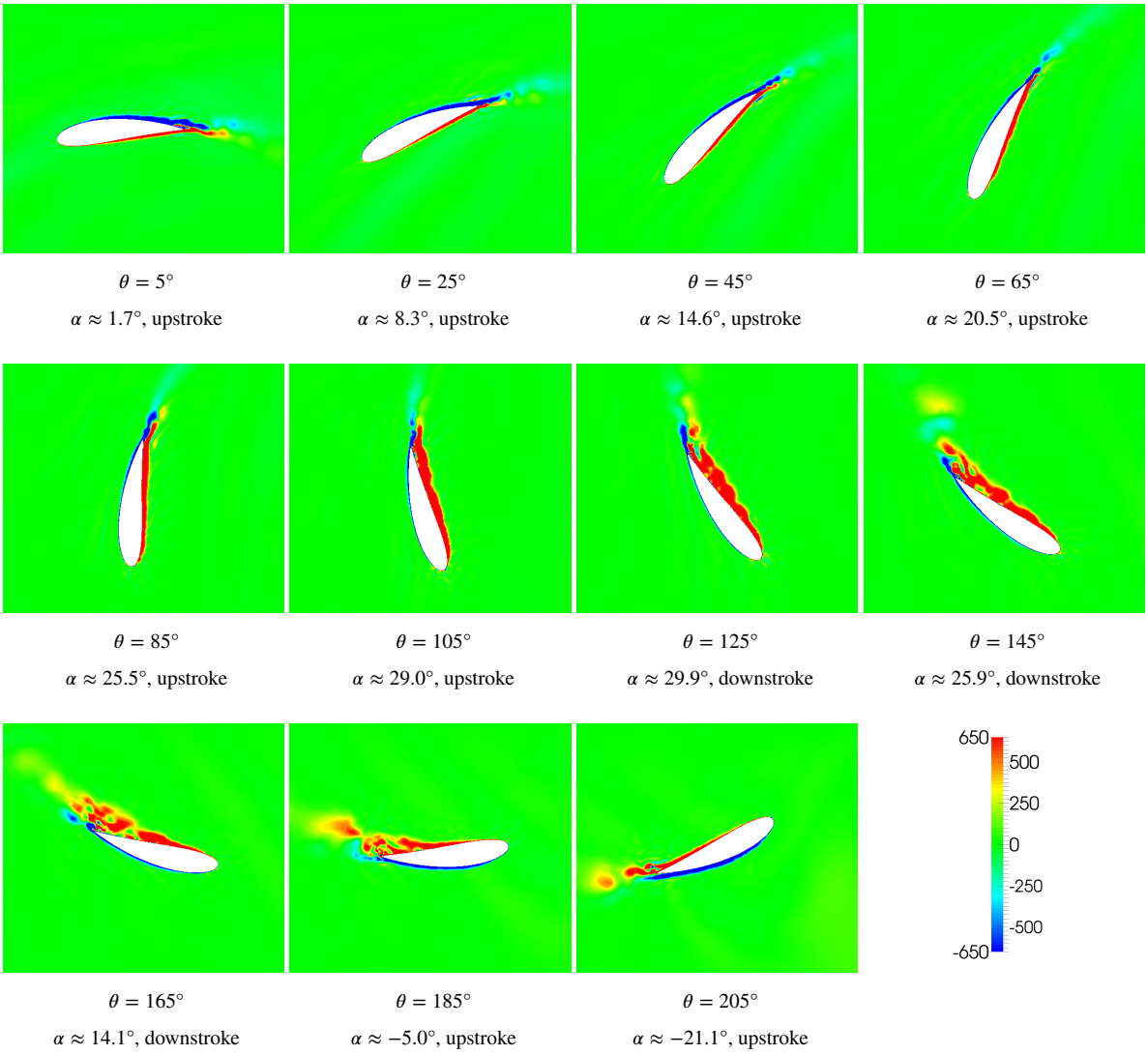

$\theta = 5°$
$\alpha \approx 1.7°$, upstroke

$\theta = 25°$
$\alpha \approx 8.3°$, upstroke

$\theta = 45°$
$\alpha \approx 14.6°$, upstroke

$\theta = 65°$
$\alpha \approx 20.5°$, upstroke

$\theta = 85°$
$\alpha \approx 25.5°$, upstroke

$\theta = 105°$
$\alpha \approx 29.0°$, upstroke

$\theta = 125°$
$\alpha \approx 29.9°$, downstroke

$\theta = 145°$
$\alpha \approx 25.9°$, downstroke

$\theta = 165°$
$\alpha \approx 14.1°$, downstroke

$\theta = 185°$
$\alpha \approx -5.0°$, upstroke

$\theta = 205°$
$\alpha \approx -21.1°$, upstroke

Figure 15: Contour of spanwise vorticity (s^{-1}) at quarter-blade height for the real turbine at $\sigma = 0.55$ and $\lambda = 2$. Angle of incidence α on the blade has been obtained with equation 1.

As the blade/arm connection of the studied geometry has been designed to reduce these interferences, the efficiency of this region is less degraded than the blade tip efficiency.

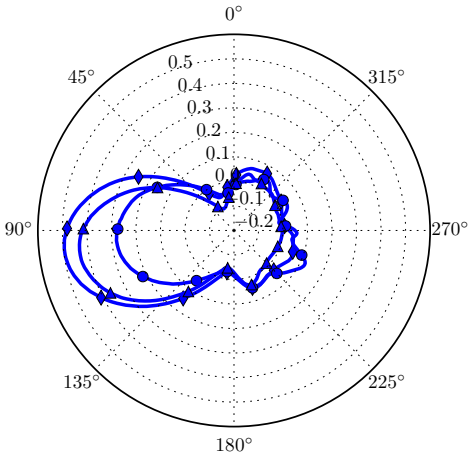

Figure 16: η^{region} as a function of angular position for the real turbine at $\sigma = 0.55$ and $\lambda = 2$. ♦: blade, ●: blade tip, ▲: blade/arm connection.

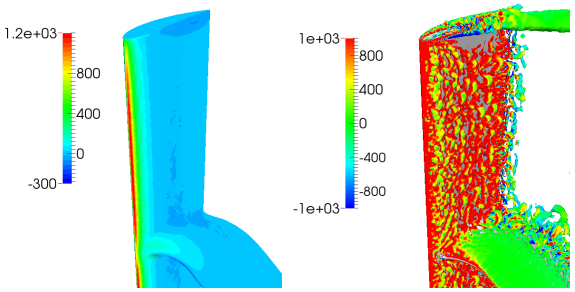

(a) (b)

Figure 17: Contour of $C_p\left(\overrightarrow{OI}\right)$ (a) and isosurface of Q-criterion, $Q = 2.25 \times 10^5 s^{-2}$, coloured by spanwise vorticity (s^{-1}) (b) along a blade at $\theta = 95°$ for the real turbine at $\sigma = 0.55$ and $\lambda = 2$.

To quantify the disturbance due the blade tip and the blade/arm connection, the efficiency of the real turbine is compared with the ideal turbine configuration in Figure 18. The efficiency of the blade region for both geometries is globally equivalent. We notice a degradation of the efficiency for the real turbine in the angular ranges $90° \leq \theta \leq 180°$ and $270° \leq \theta \leq 360°$. The blade region efficiency is consequently slightly decreased by the blade tip and the blade/arm connection region.

To end up with the analysis of the high solidity turbine ($\sigma = 0.55$) at optimal TSR ($\lambda = 2$), table 5 sums up the values of $\langle C_p^{region} \rangle$ and $\langle \eta^{region} \rangle$ for the different regions.

Region	$\langle C_p^{region} \rangle$	h^{region} (m)	$\langle \eta^{region} \rangle$
Blade (ideal)	0.0615	0.08025	0.1231
Blade	0.0320	0.05	0.1118
Blade tip	0.0068	0.0175	0.0678
Blade/arm connection	0.0079	0.02	0.0688

Table 5: $\langle C_p^{region} \rangle$ and $\langle \eta^{region} \rangle$ for $\sigma = 0.55$, $\lambda = 2$.

This part was dedicated to the analysis of the high solidity turbine at optimal TSR. The next section aims to better understand the mean power coefficient differences observed between the high and the low solidity VAHT at their optimal TSR.

4.1.3. Comparison of VAHT at $\sigma = 0.55$ and $\lambda = 2$ with VAHT at $\sigma = 0.16$ and $\lambda = 3.4$

Figure 19 shows the evolution of C_p^{region} for the blade region, the blade tip and the blade/arm connection as a function of the angular position θ for the low solidity real turbine at $\lambda = 3.4$. Contrarily to the previous observation for the high solidity turbine, the power coefficient is generated in the upstream half-disk and in the downstream half-disk. According to Figure 20, the flow blockage is lower in comparison with the high solidity turbine case. The velocities observed in the downstream half-disk are high enough to generate power. These velocities are however lower to those observed in the upstream half-disk. The

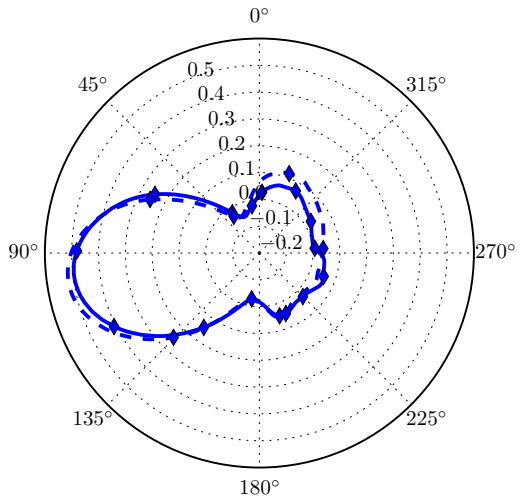

Figure 18: η^{region} as a function of angular position for the blade region at $\sigma = 0.55$ and $\lambda = 2$. ——: real turbine, – – –: ideal turbine.

maximal power coefficient generated in the downstream half-disk is consequently lower than that generated in the upstream half-disk. However, a non-zero power coefficient is obtained on a larger range of angles in the downstream half-disk.

According to equations 1 and 2, with $\sigma = 0.16$ and $\lambda = 3.4$, the reduced frequency k_{VAHT} is equal to 0.07 and the maximal angle of incidence on the blade is equal to 17.1°. The low solidity turbine blade operates either in a quasi-steady regime either with a weak dynamic stall phenomenon. As shown in Figure 21, the flow around the blade is less detached during a round. It is more pronounced in the downstream half-disk where the flow velocity is lower. The lift-to-drag ratio of the blade is consequently better in the low solidity turbine case than in the high solidity turbine case.

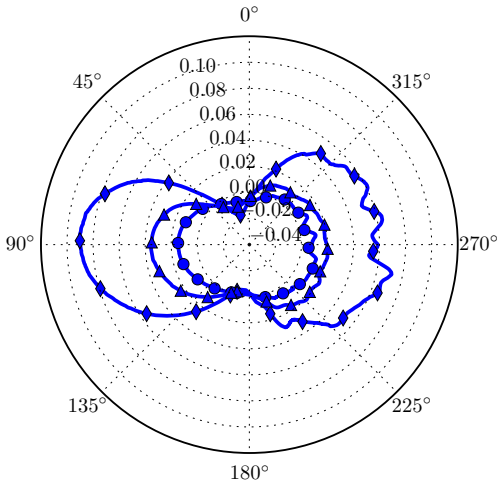

Figure 19: C_p^{region} as a function of angular position for $\lambda = 3.4$. ♦: blade, ● : blade tip, ▲: blade/arm connection.

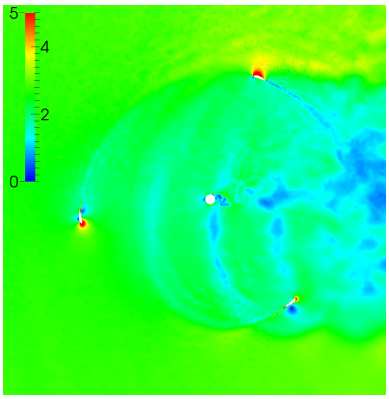

Figure 20: Slice of the computation domain at quarter-blade height colored by absolute velocity magnitude ($m.s^{-1}$).

Figure 22a shows the evolution of the instantaneous power coefficient C_p^{VAHT} for both ideal and real configurations at their optimal TSR. For the ideal turbine cases, we notice that the power coefficient of the low solidity turbine is higher for all angular

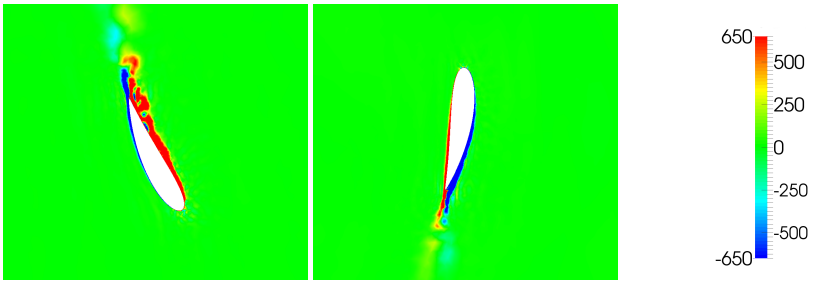

$\theta = 115°$ $\theta = 261°$

$\alpha \approx 16.9°$, downstroke $\alpha \approx -16.9°$, downstroke

Figure 21: Contour of spanwise vorticity (s^{-1}) at quarter-blade height for the real turbine at $\sigma = 0.16$ and $\lambda = 3.4$. Angle of incidence α on the blade has been obtained with equation 1.

positions. However, this is not observed for the real turbines. Depending on the angular position, the low solidity turbine generates more or less power than the high solidity turbine. Note that the power coefficient varies less during a revolution for the low solidity turbine cases whatever the geometry.

Figure 22b shows the evolution of the efficiency of the blade region as a function of angular position for high and low solidity turbines. The differences of behavior are highlighted. As already explained, for the high turbine solidity cases, the major part of the mean power coefficient is generated into the upstream half-disk. Due to a low TSR, high angles of incidence are reached. The dynamic stall phenomenon leads the blades to generate high instantaneous power coefficient values. For the low solidity turbine cases, the higher optimal TSR leads to lower angles of incidence. Despite a higher rotation speed the power coefficient generated in the upstream half-disk is lower than that of the high solidity turbine case. However, for the low solidity turbine case, the flow velocities observed in the downstream half-disk are high enough to generate a high amount of power coefficient. Consequently, for the ideal turbine cases, the mean power coefficient generated by the low solidity turbine case is strongly higher in comparison with the high solidity case.

However, as seen in Figure 22b, the efficiency of the blade region is degraded for the real turbine case compared to the ideal turbine case in the angular ranges $90° \leq \theta \leq 180°$ and $270° \leq \theta \leq 360°$. A higher gap of efficiency between the ideal and the real turbines is observed in the low solidity turbine case. The efficiency of the blade region is thus more degraded by the blade tip and the blade/arm connection in the low solidity case than in the high solidity case. According to Figure 24, it seems that the decrease of efficiency of the blade region in the low solidity real turbine is mainly due to the blade tip. A blade tip vortex is observed in Figure 25. The associated decrease of $C_p\left(\overrightarrow{OI}\right)$ values due to the leakage of streamlines seems to extend over a larger part of the blade compared to the high solidity case as seen in Figure 17a. In the ideal turbine case where there is no blade tip vortex, $C_p\left(\overrightarrow{OI}\right)$ values at the leading edge are higher and its distribution is uniform along the blade.

Figure 23a shows the evolution of C_p^{region} as a function of the angular position for the blade/arm connection and the blade tip regions. The impact of the solidity decrease on the blade/arm connection region is similar to that of the blade region. A solidity decrease leads to decrease the power coefficient generated in the upstream half-disk and to increase the power coefficient generated in the downstream half-disk. A decrease of the power coefficient in the upstream half-disk is also observed for the blade tip. However, no significant power coefficient increase is observed in the downstream half-disk. Finally, the arms contribute to decrease the global power coefficient of the low solidity real turbine. Indeed, Figure 23b shows that the arms

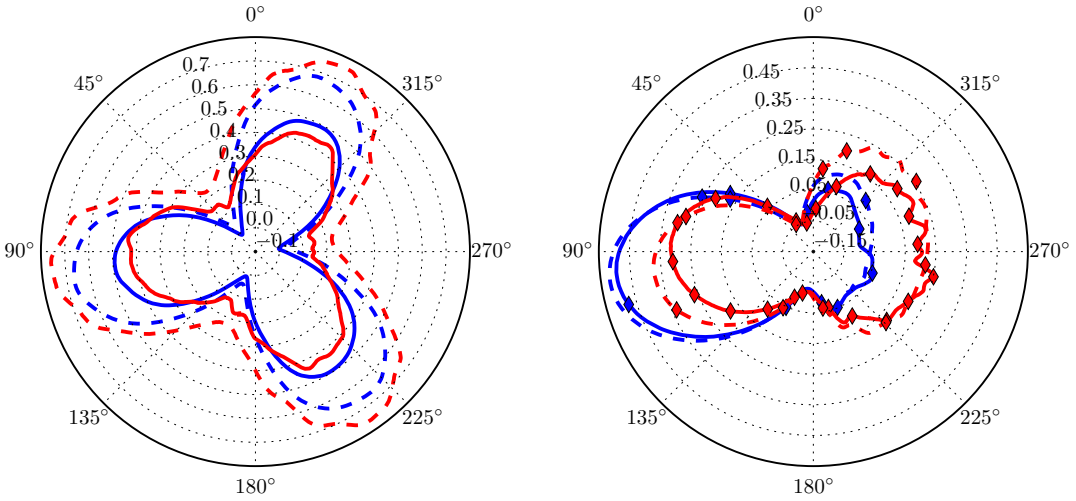

(a) (b)

Figure 22: C_p^{VAHT} (a) and η^{region} for the blade region (b) of real and ideal turbines. ——: $\sigma = 0.55$ and $\lambda = 2$, ——: $\sigma = 0.16$ and $\lambda = 3.4$. ——: real turbine, – – –: ideal turbine.

of the low solidity real turbine generate a high level of losses compared to those of the high solidity real turbine. The higher length of the arms coupled with a higher rotation speed lead to a dramatic increase of the drag of the arms.

Table 6 sums up the differences of mean regional power coefficients and mean regional efficiencies between high and low solidity turbines. In the real turbines, the potential gain of mean power coefficient due to the solidity decrease is affected by the blade tips and their impact on the rest of the blade and by the connection arms. The blade/arm connection region is less affected by the blade tip than the blade region as it is further away from the blade tip. The performance increase of the blade/arm connection region due to the solidity decrease is thus higher than that of the blade region. The efficiency increase of the blade/arm connection region is even higher than that of the blade region of the ideal turbine cases. It can be due to the lower angles of incidence reached by the blade at $\lambda = 3.4$ compared to $\lambda = 2$. It possibly leads to reduce the boundary layers interactions and the associated drag.

	$\left\langle C_p^{region} \right\rangle$			$\left\langle \eta^{region} \right\rangle$		
Region	$\sigma_1 = 0.55$	$\sigma_2 = 0.16$	$\sigma_2 - \sigma_1$	$\sigma = 0.55$	$\sigma = 0.16$	$\sigma_2 - \sigma_1$
Blade (ideal)	0.0615	0.0811	0.0196	0.1231	0.1622	0.0391
Blade	0.0320	0.0371	0.0051	0.1118	0.1299	0.0181
Blade tip	0.0068	0.0045	-0.0023	0.0678	0.0450	-0.0228
Blade/arm connection	0.0079	0.0127	0.0048	0.0688	0.1111	0.0423
Arm	≈ 0	-0.0078	-0.0078	-	-	-

Table 6: $\left\langle C_p^{region} \right\rangle$ and $\left\langle \eta^{region} \right\rangle$ for $\sigma = 0.55$ at $\lambda = 2$ and $\sigma = 0.16$ at $\lambda = 3.4$.

As seen in this section, a decrease of the turbine solidity can increase the turbine mean power coefficient, especially for an ideal turbine case. In the next section, additional ideal turbines at various solidities are investigated in order to clarify the

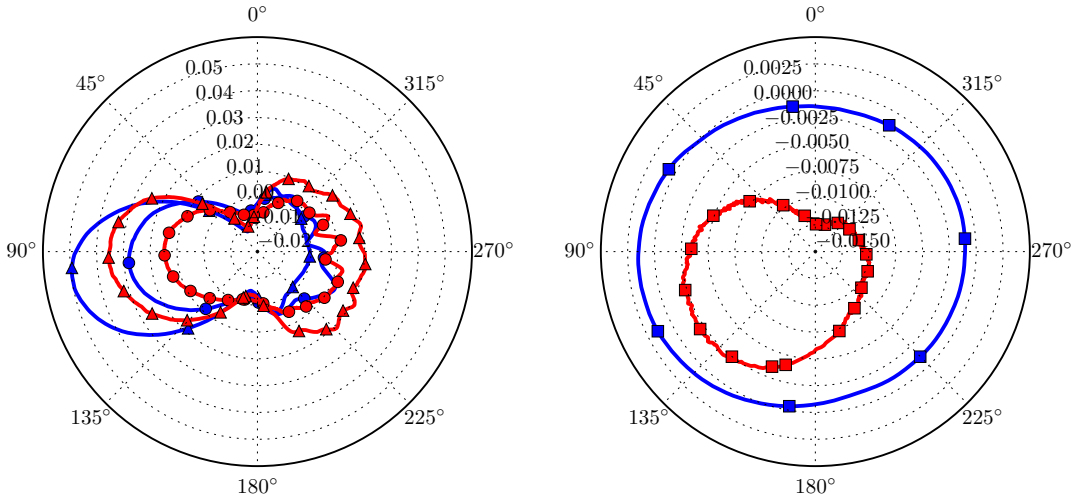

(a) (b)

Figure 23: C_p^{region} of real turbines for blade tip and blade/arm connection (a) and for arm (b) as a function of angular position. ——: $\sigma = 0.55$, ——: $\sigma = 0.16$. ● : blade tip, ▲: blade/arm connection, ■: arm.

evolution of the optimal mean power coefficient as a function of turbine solidity.

4.2. Evolution of the optimal power coefficient as a function of solidity for ideal turbines

Figure 26 shows the evolution of the optimal mean power coefficient $\left\langle C_p^{VAHT} \right\rangle$ as a function of the turbine solidity. A maximum value is observed at $\sigma = 0.16$. The turbine of higher solidity operates with a more and more pronounced dynamic stall phenomenon as the solidity increases, since the associated optimal TSR decreases. The increase of the mean power coefficient from high solidities to $\sigma = 0.16$ is gradual. No local maximum value which could appear from a particular dynamic stall regime has been observed.

For solidities lower than the optimal value, the angle of incidence on the blade becomes too low, the lift generated by the blade decreases and the projection of lift and drag on the rotation circle does not favor a positive torque, which leads to decrease the mean power coefficient.

Figure 27a shows that variations of the instantaneous power coefficient during a revolution become lower as the solidity decreases. Figure 27b shows that the power coefficient generation is concentrated in the upstream half-disk for high solidities. The power coefficient generation decreases in the upstream half-disk and increases in the downstream half disk as the solidity decreases. It becomes balanced between the upstream and the downstream half-disk at the optimal solidity $\sigma = 0.16$. When the solidity decreases more, the gain in the downstream half-disk seems to be lower than the loss in the upstream half-disk and the turbine mean power coefficient globally decreases.

5. Conclusions

Large Eddy Simulations (LES) have been performed on Vertical Axis Hydrokinetic Turbines (VAHT) in order to deeply analyze the efficiency of turbines, allowing to better understand the influence of the turbine solidity. *Real* and *ideal* turbines

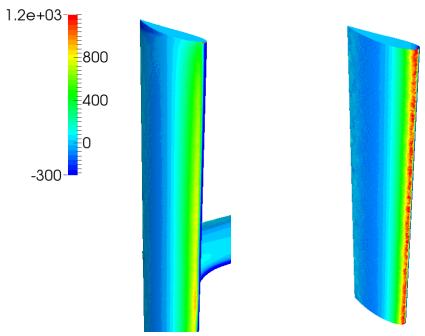

(a) (b)

Figure 24: Contour of $C_p\left(\overrightarrow{OI}\right)$ for sreal turbine (a) and ideal turbine (b) at $\theta = 335°$ for $\lambda = 3.4$, $\sigma = 0.16$.

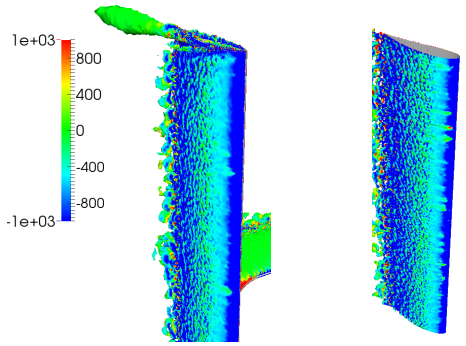

(a) (b)

Figure 25: Q-criterion isosurface, $Q = 2.25\times10^5 s^{-2}$, colored by spanwise vorticity (s^{-1}) for real turbine (a) and ideal turbine (b) at $\theta = 335°$ for $\lambda = 3.4$, $\sigma = 0.16$.

are considered. Whereas the real turbines correspond to the Achard turbine, the ideal turbines are only composed by infinite blades. This enables to evaluate the effect of major losses due to arm, shaft, blade tip, ... on the turbine performance.

Considering first the ideal turbines, for high solidity turbine cases, most of the power coefficient is generated in the upstream half-disk, $0° \leq \theta \leq 180°$, where a dynamic stall phenomenon delays the flow stall, even if the angles of incidence on the blades exceed the static stall angle. However, there is an important flow blockage with a strong decrease of flow velocity in the downstream half-disk, $180° \leq \theta \leq 360°$. Conversely, in the lower solidity cases, the optimal Tip Speed Ratio (TSR) is higher than in the high solidity turbine cases and lower incidence angles are reached. The lower solidity turbine blade consequently operates with a less pronounced dynamic stall phenomenon. A lower flow blockage is therefore observed, and the power coefficient generated by the blade is balanced between the upstream half-disk and the downstream half-disk. An optimal solidity is then found at $\sigma \approx 0.16$, leading to the optimal mean power coefficient. For lower solidities than this optimal value, incidence angles on the blade become too low and projection of lift and drag does not favor a positive torque.

Considering now the real turbines, the performance of the turbine is mainly degraded by blade tips, arm and blade/arm connections. Moreover, there is no clear gain to decrease the solidity, as observed for the ideal turbine. Because of the higher optimal TSR for smaller solidity, this is mainly due to two effects: (i) the increase of the drag of the arm, and (ii) the increase of the losses due to the blade tips. Due to these high losses, the difference of mean power coefficients between the real and the ideal turbines increases for lower solidity. The optimal solidity of a Darrieus turbine thus strongly depends on its design. For example, Shiono *et al.* [4] studied a turbine with two arms per blade and blade tips. This implies a low optimal TSR to limit losses, and they consequently found a high optimal solidity ($\sigma = 0.56$). Conversely, Blackwell *et al.* [5] investigate a turbine with a shape close to an ideal troposkien. The losses are limited and a higher optimal TSR can be reached. A lower optimal solidity situated between 0.2 et 0.25 has consequently been found. The optimization of VAHT design to limit the turbine losses is therefore of paramount importance to bring closer real VAHT optimal solidity to ideal VAHT optimal solidity and to increase the optimal mean power coefficient.

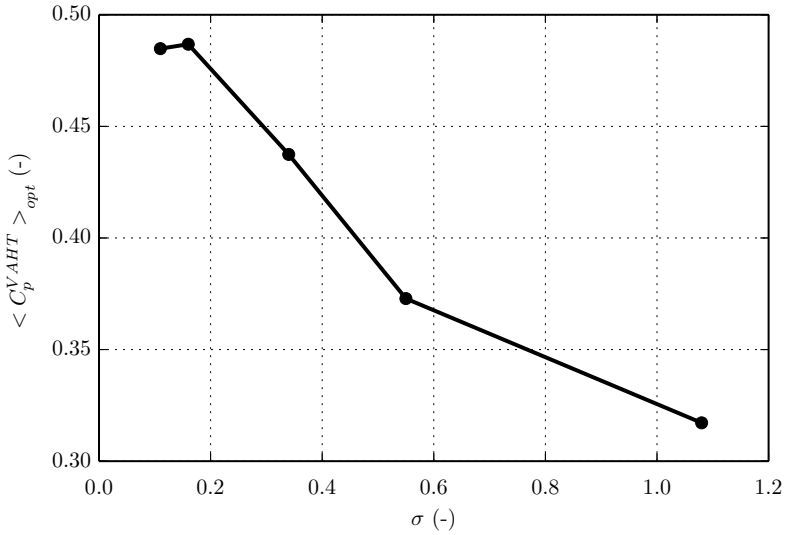

Figure 26: Optimal mean power coefficient as a function of solidity for ideal turbines.

Acknowledgments

This work has been supported by the Hydrofluv Project, a Research Program piloted by HydroQuest. Vincent Moureau and Ghislain Lartigue from the CORIA lab, and the SUCCESS scientific group are acknowledged for providing the YALES2 code. Computations presented in this paper were performed using HPC resources from GENCI (Grant No. 020611) and CIMENT infrastructure (supported by CPER07 13 CIRA and ANR-10-EQPX-29-01). Jean-Luc Achard and Stéphane Barre are acknowledged for technical discussions. Patrick Bégou is acknowledged for IT support. G.B. is also grateful for the support from Institut Universitaire de France.

References

[1] I. Bryden, S. Couch, Me1-marine energy extraction: tidal resource analysis, Renewable Energy 31 (2) (2006) 133–139.

[2] F. Dominguez, J. Achard, J. Zanette, C. Corre, Fast power output prediction for a single row of ducted cross-flow water turbines using a bem-rans approach, Renewable Energy 89 (2016) 658–670.

[3] R. Gosselin, G. Dumas, M. Boudreau, Parametric study of h-darrieus vertical-axis turbines using cfd simulations, Journal of Renewable and Sustainable Energy 8 (5) (2016) 053301.

[4] M. Shiono, K. Suzuki, S. Kiho, An experimental study of the characteristics of a darrieus turbine for tidal power generation, Electrical Engineering in Japan 132 (3) (2000) 38–47.

[5] B. Blackwell, R. Sheldahl, L. Feltz, Wind tunnel performance data for the darrieus wind turbine with naca 0012 blades, Tech. rep., Sandia Labs., Albuquerque, N. Mex.(USA) (1976).

[6] J. Zanette, Hydroliennes à flux transverse: contribution à l'analyse de l'interaction fluide-structure, Ph.D. thesis, Université de Grenoble (2010).

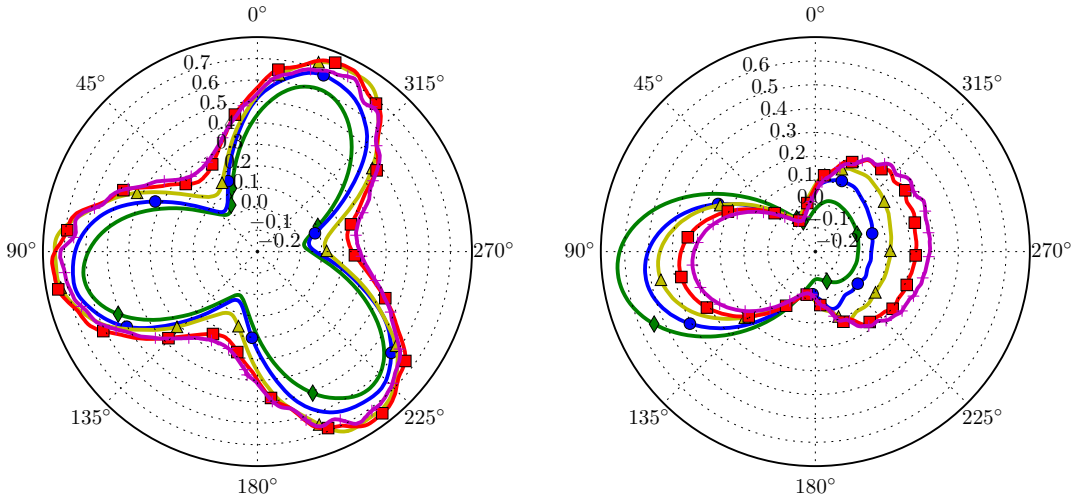

(a) (b)

Figure 27: Evolution as a function of angular position of C_p^{VAHT} (a) and C_p^{region} for the blade region (b) of ideal turbines for different solidities. ♦: $\sigma = 1.03$, ●: $\sigma = 0.55$, ▲: $\sigma = 0.34$, ■: $\sigma = 0.16$, +: $\sigma = 0.11$.

[7] I. Paraschivoiu, Wind turbine design: with emphasis on Darrieus concept, Presses inter Polytechnique, 2002.

[8] W. McCroskey, The phenomenon of dynamic stall., Tech. rep., DTIC Document (1981).

[9] P. Fraunie, C. Beguier, I. Paraschivoiu, G. Brochier, Water channel experiments of dynamic stall on darrieus wind turbine blades, Journal of Propulsion and Power 2 (5) (1986) 445–449.

[10] N. Fujisawa, S. Shibuya, Observations of dynamic stall on darrieus wind turbine blades, Journal of Wind Engineering and Industrial Aerodynamics 89 (2) (2001) 201–214.

[11] C. Simão Ferreira, G. van Kuik, G. van Bussel, F. Scarano, Visualization by piv of dynamic stall on a vertical axis wind turbine, Experiments in Fluids 46 (1) (2009) 97–108.

[12] W. McCroskey, K. McAlister, L. Carr, S. Pucci, O. Lambert, R. Indergrand, Dynamic stall on advanced airfoil sections, Journal of the American Helicopter Society 26 (3) (1981) 40–50.

[13] L. Carr, K. McAlister, W. McCroskey, Analysis of the development of dynamic stall based on oscillating airfoil experiments, Tech. rep. (1977).

[14] N. Guillaud, G. Balarac, E. Goncalvès, Large eddy simulations on a pitching airfoil: Analysis of the reduced frequency influence, Computers & Fluids 161 (2018) 1–13.

[15] A. Laneville, P. Vittecoq, Dynamic stall: the case of the vertical axis wind turbine, Journal of Solar Energy Engineering 108 (2) (1986) 140–145.

[16] C. Pellone, T. Maitre, E. Amet, 3d rans modeling of a cross flow water turbine, in: Advances in Hydroinformatics, Springer, 2014, pp. 405–418.

[17] J. Bossard, Caractérisation expérimentale du décrochage dynamique dans les hydroliennes à flux transverse par la méthode piv (particle image velocimetry). comparaison avec les résultats issus des simulations numériques, Ph.D. thesis, Université de Grenoble (2012).

[18] S. Joo, H. Choi, J. Lee, Aerodynamic characteristics of two-bladed h-darrieus at various solidities and rotating speeds, Energy 90 (2015) 439–451.

[19] A. Posa, C. Parker, M. Leftwich, E. Balaras, Wake structure of a single vertical axis wind turbine, International Journal of Heat and Fluid Flow.

[20] C. Li, S. Zhu, Y. Xu, Y. Xiao, 2.5 d large eddy simulation of vertical axis wind turbine in consideration of high angle of attack flow, Renewable energy 51 (2013) 317–330.

[21] M. Breuer, N. Jovičić, K. Mazaev, Comparison of des, rans and les for the separated flow around a flat plate at high incidence, International Journal for Numerical Methods in Fluids 41 (4) (2003) 357–388.

[22] P. H, Large-eddy simulation of turbulent combustion, Annual Review of Fluid Mechanics 38 (2006) 453–482. doi:10.1146/annurev.fluid.38.050304.092133.

[23] J. Santiago, A. Dejoan, A. Martilli, F. Martin, A. Pinelli, Comparison between large-eddy simulation and reynolds-averaged navier–stokes computations for the must field experiment. part i: study of the flow for an incident wind directed perpendicularly to the front array of containers, Boundary-layer meteorology 135 (1) (2010) 109–132.

[24] M. Liu, L. Tan, S. Cao, Cavitation–vortex–turbulence interaction and one-dimensional model prediction of pressure for hydrofoil ale15 by large eddy simulation, Journal of Fluids Engineering 141 (2) (2019) 021103.

[25] J. Decaix, G. Balarac, M. Dreyer, M. Farhat, C. Münch, Rans and les computations of the tip-leakage vortex for different gap widths, Journal of turbulence 16 (4) (2015) 309–341.

[26] Y. Tominaga, T. Stathopoulos, CFD modeling of pollution dispersion in a street canyon: Comparison between LES and RANS, Journal of Wind Engineering and Industrial Aerodynamics 99 (4) (2011) 340–348.

[27] G. Constantinescu, W. Krajewski, C. Ozdemir, T. Tokyay, Simulation of airflow around rain gauges: Comparison of les with rans models, Advances in Water Resources 30 (1) (2007) 43–58.

[28] Y. Liu, P. G. Tucker, G. L. Iacono, Comparison of zonal rans and les for a non-isothermal ribbed channel flow, International Journal of Heat and Fluid Flow 27 (3) (2006) 391–401.

[29] Y. Chang, A. Scotti, Modeling unsteady turbulent flows over ripples: Reynolds-averaged navier-stokes equations (rans) versus large-eddy simulation (les), Journal of Geophysical Research: Oceans 109 (C9).

[30] S. Rhea, M. Bini, M. Fairweather, W. Jones, RANS modelling and LES of a single-phase, impinging plane jet, Computers & Chemical Engineering 33 (8) (2009) 1344–1353.

[31] J. Achard, T. Maître, Hydraulic turbomachine (Nov. 2006).
URL https://hal.archives-ouvertes.fr/hal-00189351

[32] N. Dellinger, Instrumentation d'un tunnel hydrodynamique pour la caractérisation de turbines à flux transverse, Ph.D. thesis, Université de Grenoble (2011).

[33] A. Mentxaka Roa, V. Aumelas, T. Maître, C. Pellone, Numerical and experimental analysis of a darrieus-type cross flow water turbine in bare and shrouded configurations, in: IOP Conference Series: Earth and Environmental Science, Vol. 12, IOP Publishing, 2010, p. 012113.

[34] L. Beaudet, Etude expérimentale et numérique du décrochage dynamique sur une éolienne à axe vertical de forte solidité, Ph.D. thesis, Université de Poitiers (2014).

[35] J. Hunt, A. Wray, P. Moin, Eddies, streams, and convergence zones in turbulent flows.

[36] P. Sagaut, Large Eddy Simulation for Incompressible Flows: An Introduction, Springer Science & Business Media, 2006.

[37] V. Moureau, P. Domingo, L. Vervisch, Design of a massively parallel cfd code for complex geometries, Comptes Rendus Mécanique 339 (2) (2011) 141–148.

[38] A. Chorin, Numerical solution of the navier-stokes equations, Mathematics of computation 22 (104) (1968) 745–762.

[39] M. Malandain, N. Maheu, V. Moureau, Optimization of the deflated conjugate gradient algorithm for the solving of elliptic equations on massively parallel machines, Journal of Computational Physics 238 (2013) 32–47.

[40] M. Kraushaar, Application of the compressible and low-mach number approaches to large-eddy simulation of turbulent flows in aero-engines, Ph.D. thesis, Institut National Polytechnique de Toulouse-INPT (2011).

[41] V. Moureau, P. Domingo, L. Vervisch, From large-eddy simulation to direct numerical simulation of a lean premixed swirl flame: Filtered laminar flame-pdf modeling, Combustion and Flame 158 (7) (2011) 1340–1357.

[42] L. Guedot, G. Lartigue, V. Moureau, Design of implicit high-order filters on unstructured grids for the identification of large-scale features in large-eddy simulation and application to a swirl burner, Physics of Fluids (1994-present) 27 (4) (2015) 045107.

[43] C. Chnafa, S. Mendez, F. Nicoud, Image-based large-eddy simulation in a realistic left heart, Computers & Fluids 94 (2014) 173–187.

[44] S. Wilhelm, G. Balarac, O. Métais, C. Ségoufin, Analysis of head losses in a turbine draft tube by means of 3d unsteady simulations, Flow, Turbulence and Combustion 97 (4) (2016) 1255–1280.

[45] P. Benard, A. Viré, V. Moureau, G. Lartigue, L. Beaudet, P. Deglaire, L. Bricteux, Large-eddy simulation of wind turbines wakes including geometrical effects, Computers & Fluids 173 (2018) 133–139.

[46] N. Odier, G. Balarac, C. Corre, Numerical analysis of the flapping mechanism for a two-phase coaxial jet, International Journal of Multiphase Flow 106 (2018) 164–178.

[47] M. Germano, U. Piomelli, P. Moin, W. Cabot, A dynamic subgrid-scale eddy viscosity model, Physics of Fluids A: Fluid Dynamics (1989-1993) 3 (7) (1991) 1760–1765.

[48] M. Liu, L. Tan, Y. Liu, Y. Xu, S. Cao, Large eddy simulation of cavitation vortex interaction and pressure fluctuation around hydrofoil ale 15, Ocean Engineering 163 (2018) 264–274.

[49] M. Werle, Wind turbine wall-blockage performance corrections, Journal of Propulsion and Power 26 (6) (2010) 1317–1321.

[50] N. Guillaud, G. Balarac, E. Goncalvès, J. Zanette, Large eddy simulations on vertical axis hydrokinetic turbines and flow phenomena analysis, in: IOP Conference Series: Earth and Environmental Science, Vol. 49, 2016, p. 102010.

[51] T. Lee, P. Gerontakos, Investigation of flow over an oscillating airfoil, Journal of Fluid Mechanics 512 (2004) 313–341.